A preliminary case study of the effect of shoe-wearing on the biomechanics of a horse's foot

Olga Panagiotopoulou, Jeffery W Rankin, Stephen M Gatesy, Hyab Mehari Abraha, Jan Janzekovic, John R Hutchinson

Horse racing is a multi-billion-dollar industry that has raised welfare concerns due to disabled and euthanized animals. Whilst the cause of musculoskeletal injuries that lead to horse morbidity and mortality is multifactorial, pre-existing pathologies, increased speeds and substrate of the racecourse are likely contributors to foot disease. The hooves of horses have the ability to naturally deform during locomotion and dissipate locomotor stresses, yet farriery approaches are utilised to increase performance and protect hooves from wear. Previous studies have assessed the effect of different shoe designs on locomotor performance; however, no biomechanical study has hitherto measured the effect of horseshoes on the stresses of the foot skeleton in vivo. As there is a need to reduce musculoskeletal injuries in racing and training horses, it is crucial to understand the natural function of the feet of horses and how this is influenced by shoe design. This preliminary study introduces a novel combination of three-dimensional data from biplanar radiography, inverse dynamics, and finite element analysis (FEA) to evaluate the effect of a stainless steel shoe on the function of a Thoroughbred horse's front foot during walking. Our results show that the stainless steel shoe increases craniocaudal, mediolateral and vertical GRFs at mid-stance. We document a similar pattern of flexion-extension in the PIP (pastern) and DIP (coffin) joint between the unshod and shod conditions, yet variation in the degrees of rotations are encountered throughout the stance phase. In particular, in both the shod and unshod conditions, the PIP joint extends between the 10-40% of the stance phase and flexes before mid-stance and until the end of the stance phase. Similarly the DIP joint extends until the 40% of stance and then flexes until the end of the stance phase. Overall at mid-stance the PIP joint extends more at the shod (-2.9o) than the unshod (-1.5o) horse, whilst the DIP joint extends more at the unshod (-3.6o), than the shod (-2.8o) condition. We also document that the DIP joint flexes more than the PIP after mid-stance and until the end of the stance in both conditions. Our FEA results show increased von Mises stresses on the fore foot phalanges in the shod condition at mid-stance, indicating that the steel shoe increases mechanical loading. Our preliminary study illustrates how the shoe may influence the dynamics and mechanics of a Thoroughbred horse's forefoot during slow walking, but more research is needed to quantify the effect of

PeerJ PrePrints | https://doi.org/10.7287/peerj.preprints.1779v1 | CC-BY 4.0 Open Access | rec: 23 Feb 2016, publ: 23 Feb 2016

the shoe on the equine forefoot during the whole stance phase, at faster speeds/gaits and with more individuals as well as with a similar focus on the hind feet. We anticipate that our preliminary analysis using advanced methodological approaches will pave the way for new directions in research on the form/function relationship of the equine foot, with the ultimate goal to minimise foot injuries and improve animal health and welfare.

A preliminary case study of the effect of shoe-wearing on the biomechanics of a horse's foot

Olga Panagiotopoulou[1, 2], Jeffery W. Rankin[1], Stephen M. Gatesy[3], Hyab Mehari Abraha[2], Jan Janzekovic[2], John R. Hutchinson[1, 2]

[1]Department of Comparative Biomedical Sciences, Royal Veterinary College, Hatfield, United Kingdom.

[2]School of Biomedical Sciences, The University of Queensland, Brisbane, Australia.

[3]Department of Ecology and Evolutionary Biology, Brown University, Providence, Rhode Island, USA.

Corresponding Authors:

Dr. Olga Panagiotopoulou

Moving Morphology and Functional Mechanics Laboratory, School of Biomedical Sciences, The University of Queensland, Room 433-Otto Hirschfeld Building (81), Brisbane, QLD 4072, Australia.

o.panagiotopoulou@uq.edu.au

Prof. John R Hutchinson

Structure & Motion Laboratory, The Royal Veterinary College, Hawkshead Lane, North Mymms, Hatfield, AL9 7TA, United Kingdom.

jhutchinson@rvc.ac.uk

Abstract

Horse racing is a multi-billion-dollar industry that has raised welfare concerns due to disabled and euthanized animals. Whilst the cause of musculoskeletal injuries that lead to horse morbidity and mortality is multifactorial, pre-existing pathologies, increased speeds and substrate of the racecourse are likely contributors to foot disease. The hooves of horses have the ability to naturally deform during locomotion and dissipate locomotor stresses, yet farriery approaches are utilised to increase performance and protect hooves from wear. Previous studies have assessed the effect of different shoe designs on locomotor performance; however, no biomechanical study

has hitherto measured the effect of horseshoes on the stresses of the foot skeleton *in vivo*. As there is a need to reduce musculoskeletal injuries in racing and training horses, it is crucial to understand the natural function of the feet of horses and how this is influenced by shoe design. This preliminary study introduces a novel combination of three-dimensional data from biplanar radiography, inverse dynamics, and finite element analysis (FEA) to evaluate the effect of a stainless steel shoe on the function of a Thoroughbred horse's front foot during walking. Our results show that the stainless steel shoe increases craniocaudal, mediolateral and vertical GRFs at mid-stance. We document a similar pattern of flexion-extension in the PIP (pastern) and DIP (coffin) joint between the unshod and shod conditions, yet variation in the degrees of rotations are encountered throughout the stance phase. In particular, in both the shod and unshod conditions, the PIP joint extends between the 10-40% of the stance phase and flexes before mid-stance and until the end of the stance phase. Similarly the DIP joint extends until the 40% of stance and then flexes until the end of the stance phase. Overall at mid-stance the PIP joint extends more at the shod (-2.9°) than the unshod (-1.5°) horse, whilst the DIP joint extends more at the unshod (-3.6°), than the shod (-2.8°) condition. We also document that the DIP joint flexes more than the PIP after mid-stance and until the end of the stance in both conditions. Our FEA results show increased von Mises stresses on the fore foot phalanges in the shod condition at mid-stance, indicating that the steel shoe increases mechanical loading. Our preliminary study illustrates how the shoe may influence the dynamics and mechanics of a Thoroughbred horse's forefoot during slow walking, but more research is needed to quantify the effect of the shoe on the equine forefoot during the whole stance phase, at faster speeds/gaits and with more individuals as well as with a similar focus on the hind feet. We anticipate that our preliminary analysis using advanced methodological approaches will pave the way for new directions in research on the form/function relationship of the equine foot, with the ultimate goal to minimise foot injuries and improve animal health and welfare.

Introduction

Horse racing is a multi-billion-dollar, worldwide industry in which the welfare of the horses is of paramount importance. Musculoskeletal injuries are both a common cause of economic loss within the industry and a major welfare concern due to the resulting morbidity and mortality (McKee 1995; Jeffcott et al., 1982; Clegg 2011; Bailey et al., 1999). The causes of musculoskeletal injuries is multifactorial: pre-existing pathologies, increased speeds, and track surfaces are all recognised as contributing factors (Parkin et al., 2004; Cogger et al., 2006; Foote et al., 2011; Clegg 2011). Horses have evolved to only maintain their third digit, which ends in a rigid hoof capsule and is functionally adapted to fast speeds (Dyce et al., 2010). The hoof and the interphalangeal joints receive most of the impact loads when the foot hits the ground (Dyhre-Poulsen et al., 1994) and at fast speeds these loads can exceed 2.5 times the horse's body weight (Witte et al., 2004). Under load-bearing conditions, the distal and coronary borders of the hooves expand (Colles 1989); the dorsal hoof wall rotates caudoventrally about the third digit and the heel expands between 2-4mm (Jordan et al., 2001). The exact mechanisms under which the hooves expand are still obscured, yet the friction between the hoof and the ground resulting from this expansion during locomotion causes hoof wear and may induce foot pathology due to uneven loading if conformational abnormalities exists.

Farriery (horseshoe design) approaches in both domestic and racehorses have been used since the domestication of horses to protect hooves from wear and to allow manipulation of the shape of the foot to improve performance and enhance biomechanical function. Nevertheless, different horseshoe materials have varying effects on horses' feet due to their wide range of weight, toe angle, frictional and damping properties and their interaction with foot trimming (Roepstorff , Johnston & Drevemo 1999; Pardoe et al., 200; van Heel et al., 2005; van Heel, van Weeren &, Back 2006; Heidt et al., 1996, Willemen, Savelberg & Barneveld 1998; Balch, Clayton & Lanovaz 1996). Previous *in vivo* studies in horses have shown that an elevation of the hoof due to the presence of the shoe increases the pressure within the distal interphalangeal joint, which may account for an increase of bone stresses that can enhance the development of degenerative joint diseases (Roepstorff , Johnston & Drevemo 1999). Whilst no biomechanical study to date has quantified bone stresses of the horse forefoot in the shod and unshod conditions *in vivo*, Moyer and Anderson (1975) hypothesised that increased loading due to farriery can increase stresses on the horse foot and lead to injuries (Moyer & Anderson 1975). In addition, an *ex vivo* analysis by Ault et al., (2015) recorded significant increases in the strain of the superficial digital flexor tendon (SDFT) and the suspensory ligament of shod horses, further supporting the inference that shoes disrupt the natural ability of horses' feet to maintain tendon (and perhaps other tissue) strains at lower levels.

Whilst shoes impact the function of the equine digit, current knowledge of the relationships between foot function, farriery approaches and musculoskeletal injuries is limited, partly due to the lack of an *in vivo* experimental protocol for studying foot dynamics and mechanics. Finite element analysis (FEA) is a numerical technique well entrenched in equine biomechanics as a tool to measure deformation (stress, strain) in complex continuous systems (such as the hoof), by dividing them into sub-regions of finite size (elements) using linear ordinary differential equations (Hutton 2003). With FEA, scientists have managed to study the deformations of anatomically deep structures of the equine distal foot in shod and unshod conditions (Hinterhofer, Stanek & Haider 2001; Hinterhofer, Stanek &Binder 1998; Bowker et al., 2001; Salo, Runciman & Thomason 2009; O'Hare et al., 2013; Thomason et al., 2001, 2002, 2005; McClinchey, Thomason & Jofriet 2003; Collins et al., 2009; Douglas et al., 1998). Whilst these studies have enhanced our understanding on how the equine digit deforms under load-bearing, more robust *in vivo* data and subject-specific models are needed to fully characterize how the equine distal limb's functional environment relates to disease. This requires combining precise joint motion and ground reaction force (GRF) data from a synchronised time sequence with subject specific bone geometry. Here we show how a combination of different techniques can be used to obtain these data and generate high fidelity FEA results.

A common approach for researchers to measure joint motion in horses is the attachment of motion analysis markers on the skin overlying bony structures. This approach introduces errors, due to artifacts from skin and hoof motion, which can be as large as the actual joint motion (Reinschmidt et al., 1997; Roach et al., 2015). One alternative to surface skin markers is the surgical implantation of intra-cortical bone pins into the limb bones, but is highly invasive (e.g. Clayton et al., 2004, 2007a; van Weeren, van den Bogert & Barneveld 1990; Chateau, Degueurce & Denoix 2004). Although these pins can more accurately quantify bone motion, their invasiveness may affect the natural function/behaviour of the joints (Lundberg et al., 1989) and are inappropriate to use in requiring a large number of horse participants. Fortunately, a new alternative technology using biplanar radiography, commonly referred to as X-ray Reconstruction of Moving Morphology or XROMM, has been developed that can be used to accurately characterize the three-dimensional (3D) motion of joints (Brainerd et al., 2010; Gatesy et al., 2010).

XROMM combines bi-planar fluoroscopic images to track dynamic functions such as trotting, which enables precise measurements of joint motion without artifacts from soft tissue motion (e.g., Miranda et al., 2013). By acquisition of fluoroscopic images in two planes and with the assistance of specialised software, the images can be combined to track motion of individual skeletal elements in three dimensions. Thus, motion can be assessed *in vivo*, without the requirement for attachment of any device to the skin or into the bones. Natural behaviour can be measured in a manner not possible with other techniques and with minimal risk to the animal/participant, while keeping radiation doses reasonably low. To date, XROMM technology has been used to study diverse behaviours such as the limb kinematics of birds, bats and dogs;

jaw kinematics during feeding in fish, pigs, birds and bats and rib kinematics of breathing in lizards (e.g., Dawson et al., 2011; Gidmark et al., 2012, 2013; Metzger et al., 2009; Baier et al., 2013) (http://www.xromm.org/).

This study presents a novel method that combines three-dimensional data from XROMM (Brainerd et al., 2010; Gatesy et al., 2010), inverse dynamics, and finite element analysis to perform a preliminary investigation of the effect of a stainless steel shoe on the function of a Thoroughbred horse's foot during walking. The intent of this work is not to draw clinical conclusions on the effect of the shoe on the equine foot mechanics. Instead, we present an experimental approach that can be used in future research to expand on the effect of different shoe designs on foot mechanics and potentially inform the design of new shoes that can improve locomotor performance while maintaining the integrity of musculoskeletal structures. This should improve horse welfare, which would be of economic benefit to the racing industry, as well as providing fundamental insights into the normal functions of unshod equine feet.

Materials & Methods

Subjects

One Thoroughbred healthy male adult horse (540 kg body mass) from the Royal Veterinary College (RVC) participated in the study. The horse had previously been trained for and participated in locomotor studies in the laboratory. Fifteen minutes of training were provided for the horse to adapt to the experimental setup. The study was reviewed and approved by the Royal Veterinary College's Ethics and Welfare Committee (approval number URN 2011 1094).

Data Collection

Each trial lasted two to four seconds, during which the horse was led across a custom-designed platform (Figure 1A). A custom-designed platform rather than a treadmill was used for this study because our methodological approach for the *in vivo* estimation of the intersegmental forces for FEA required accurate ground reaction force (GRF) measurements. Accurate measurements of all GRF force components could not be obtained using any available treadmill.

A Sony HDR (Sony, London, UK) high definition video camera was placed perpendicular to the platform to approximate walking speed (25 Hz). To obtain foot kinematics, two custom x-ray fluoroscopes (RSTechnics, Netherlands; refurbished Phillips systems, 36cm intensifier; ≤110kV, ≤3mA) were retrofitted with two AOS high-speed digital cameras (AOS Technologies AG, Switzerland) to acquire biplanar fluoroscopy images at 250Hz of the horse's feet as it walked through an undistorted (see Supp. Info, Image Undistortion) and calibrated (see Supp. Info, Calibration) capture volume (~30 cm per cube edge) located on the force plate. Exposure settings were set to 69kV, 53mA and 72kV, 54mA for the two sources. Each intensifier was placed 2 metres from its corresponding x-ray source, and the systems were placed laterally to the platform in a diagonal alignment (Figure 1A).

Kinetic data were collected simultaneously at a rate of 1000 Hz using a forceplate (60x90cm with Hall Effect sensors, 2000lb peak vertical force; AMTI, Watertown, MA, USA). Prior to analysis, the forceplate data were low-pass filtered using a 4^{th} order zero-lag Butterworth filter with a cutoff frequency of 15Hz. All data were synchronized with the fluoroscope system.

The unshod horse was guided 344 times across the experimental platform. The horse was then given a two hour break, received mild foot trimming to balance the shoe on the forefeet and was fitted with a stainless steel fullered concaved wither with toe clips (5 inch wide) and 6 nails. Shoes were fitted solely to the forefeet. The identical procedure was then followed to guide the shod horse over the platform 65 times. The difference in trial numbers between the unshod (344 strides) and the shod (65 strides) conditions was due to the large number of spatially incomplete data for the former. Strides that were spatially incomplete (i.e., the right forefoot only stepped partially within the capture volume) and/or unsteady (i.e., with evident deceleration and acceleration following observation of the video images during data collection) were excluded from further analysis. Four steps from the shod and four steps from the unshod right forefoot that were spatially complete and steady were processed using the markerless XROMM (X-ray Reconstruction of Moving Morphology: Brainerd et al., 2010; Gatesy et al., 2010) workflow to construct a model and obtain 3D joint rotations and translations. The limited number of steps per conditions is a limitation of the XROMM approach when used in live animal studies for species as large as a Thoroughbred horse. For a step to be valid during the XROMM procedure, the animal has to step within the refined field of view with no deviation. If there were minimal deviations from the capture volume, we were unable to visualise the distal right forefoot in both cameras in order to extract the 3D joint kinematics.

Model Construction

The horse was euthanized at the end of the experiment for unrelated studies and its right forelimb was removed and frozen (-20° C). Computed tomography scans (GE Lightspeed 16-detector unit; General Electric) were used to obtain the three dimensional (3D) skeletal geometry of the horse's forefoot (slice thickness 0.625mm, 0.460 pixels mm^{-1}, 512x512 pixel images, 620 slices). These data were then processed to extract solid 3D polygonal mesh objects in Mimics (version 16.0; Materialise, Inc, Leuven, Belgium) and then imported into Maya (Autodesk, San Rafael, California, USA) to construct the biomechanical models' segments (Figure 1B). Four segments were defined: the metacarpus (MC), first phalanx (P1), intermediate phalanx (P2) and distal phalanx (P3). An articulated skeleton was then created by hierarchically linking these segments (Gatesy et al., 2010) into a kinematic chain using the metacarpophalangeal (MCP), proximal interphalangeal (PIP) and distal interphalangeal (DIP) joints (Figure 2).

Joint orientations and positions were defined by first positioning all bone segments into a neutral anatomical pose (forefoot lying fully horizontally). Cylinders were then visually fit to the joint surfaces (i.e., the distal epiphyses of the MC, P1 and P2) to identify the axes of joint rotations. These locations were confirmed when manual manipulation of the virtual joint resulted in a natural motion where adjacent bones did not interpenetrate each other. Dissected cadaveric specimens and plastic models were used to further confirm joint locations and positions. Transformations between coordinate systems were defined using an X (red axis), Y' (green axis), Z'' (blue axis) cardan rotation, respectively representing long axis rotation, flexion-extension, and abduction-adduction (Figure 2). Axes were defined so that positive joint angles represented external rotation, extension, and adduction.

Markerless XROMM

Trajectories for each joint were quantified using protocols established by the XROMM Research Coordination Network (Brown University, USA; www.xromm.org) for scientific rotoscoping (markerless XROMM) (Gatesy et al., 2010; Baier & Gatesy 2013; Baier et al., 2013; Nyakatura & Fischer 2010). In brief, markerless XROMM is a technique that allows one to quantify 3D motion by animating model segments (i.e., 3D polygonal mesh objects) to match postures observed in experimental x-ray video images (Figure 1B). For each experimental x-ray trial, the horse foot model was aligned with the bone x-ray silhouettes in undistorted and calibrated video images using the anatomical features of each bone as reference guides (Supplementary movies 1 & 2). Joint transformations (i.e., joint rotations and translations) were then extracted from the model for the MCP, PIP and DIP joints (Figure 2). The MCP kinematic data were excluded from further analysis because the midshaft and proximal epiphysis were out of the field of view for most of the stride.

All steps for shod (n=4) and unshod (n=4) conditions were used to measure joint kinematics and foot kinetics, but a single representative step was selected for each condition (shod n=1;

unshod n=1) for the subsequent mid-stance inverse dynamics calculations and FEA used to estimate bone stresses in the right forefoot digit.

Inverse Dynamics Analysis

Intersegmental forces (required for estimating the stresses on bones) were calculated at mid-stance for the two steps selected for analysis (shod and unshod conditions) using inverse dynamics. To perform the analysis, the skeletal model created for scientific rotoscoping was recreated in Software for Interactive Musculoskeletal Modeling (SIMM; Musculographics, California, USA). To create an exact replica of the original model, bone geometry was exported directly from Maya and imported into SIMM, where they were reassembled by reproducing the original joint structure (i.e., number of joints and degrees of freedom). The model was then exported into OpenSim (Delp et al., 2007), which has a built-in routine to perform inverse dynamics analysis.

Mid-stance was defined as the point halfway between foot strike and toe-off gait events, which were determined from the vertical GRF data. Mid-stance joint angles were exported directly from the XROMM workflow and used to position the model in OpenSim. Mid-stance GRF, obtained from the synchronized force plate data, were transformed into the same reference frame as the OpenSim foot model using custom scripts in MatLab (Mathworks, Inc., Natick, MA, USA). Ground reaction forces were then applied to the distal phalanx (P3). Data integrity between the motion and force data were verified by visually inspecting the location of the centre of pressure (CoP) (from forceplate data) relative to the foot placement (from XROMM kinematics) using OpenSim. OpenSim's inverse dynamics and joint reaction force analysis routines were then used to calculate the intersegmental joint forces and moments acting on the segments at each joint. These data were expressed in the local frame of the segment and used as inputs into the FEA.

Finite Element Analysis

For each phalanx (P1, P2 and P3), a finite element model was created in Abaqus/CAE, software version 6.13 (Dassault Systemes Simulia Corp, Providence, Rhode Island, USA). The corresponding intersegmental forces were then applied to each bone and stress was determined using the Abaqus/Standard implicit direct default solver.

<u>Bone Models</u>

The 3D bone meshes representing the segments from the OpenSim model were imported into 3-Matic 9.0 software (Materialize Inc., Leuwen, Belgium) and converted into volumetric mesh files of continuum linear tetrahedral elements of type C3D3. All volumetric mesh files (preserving the coordinate systems of each segment as defined during the inverse dynamics analysis) were then imported into Abaqus/CAE 6.13 FEA software and converted into 10 node quadratic hybrid elements of type C3D10H. The element nominal size for all models was 2mm. The P1, P2 and P3 segments had 60,967; 42,401 and 35,725 elements respectively.

Material Properties

Due to a lack of specific material properties data for the bones of the distal foot of horses, linear elasticity, homogeneity and isotropy were assumed. Assumptions regarding isotropy and homogeneity should create a constant error between our models and thus do not influence bone stress comparisons between the shod and the unshod horse. We assigned a Young's modulus (E) value of 16,000 MPa and Poisson's ratio (v) of 0.3 to the P1 and P2. The P3 in horses consists of dense trabeculae and was thus assigned a modulus of 10,000 MPa and Poisson's ratio of 0.3 (Rho et al., 2001; Jansová et al., 2015).

Loads and constraints

To load the models we applied the intersegmental forces calculated during the inverse dynamics routine for the shod and the unshod horse to the surface of the bone segments related to the joint of interest. The P1 bone was loaded at the (distal) MCP joint (Supplementary Figure S2). The P2 bone was loaded at the (distal) PIP joint (Supplementary Figure S2) and the P3 bone was loaded at the (distal) DIP joint (Supplementary Figure S2). All phalanges were constrained distally. Constraints included fixed rotations and displacements about all axes. We measured von Mises stress magnitudes from a group of external and internal elements at the midshaft in the middle transverse plane of all bone segments for the shod (n=1) and unshod (n=1) conditions (Supplementary Figure S3) and calculated the mean, minimum, maximum and standard deviation of the sample elements for each bone.

Data analysis was carried out using R v3.1.1 (R Development Core Team, Auckland, New Zealand) software. Stance phase kinetic and kinematic data were normalised to 100% stance phase duration (i.e. ground contact time). Descriptive statistics were used to quantify the walking speed within the shod (n=4) and the unshod (n=4) conditions. A cross-correlation analysis was conducted to assess the correlation between the unshod and shod horse in overall mean GRF patterns (in the craniocaudal, mediolateral and vertical directions) and the overall pattern in mean angle of flexion-extension for the PIP and DIP joints across the stance phase (10-90%). The first and last 10% of the stance phase were excluded from the kinematics data due to noise caused during markerless XROMM. Analysis of FEA involved calculating the percentage difference in mean regional von Mises stress between the shod (n=1) and unshod (n=1) conditions for the P1, P2 and P3.

Results

Speed Data

The mean walking speed of the shod and unshod conditions was at 0.72 ms^{-1} and 0.76ms^{-1} respectively (Table 1). This corresponded to a Froude number (Alexander & Jayes, 1983; F = velocity^2 * [9.81 ms^{-2} * hip height]$^{-1}$) of 0.05 for the shod condition and 0.06 for the unshod condition (Table 1), indicative of a slow walk, and the footfall patterns maintained the usual lateral sequence (Supplementary Data 1).

Kinetic Data

The GRF data from the shod (n=4) and unshod (n=4) conditions during the stance phase of locomotion are shown in Figure 3 and Supplementary Data 2. In all directions the force pattern was quite similar between the shod and unshod conditions (Figure 3). The results from the cross-correlation analysis assessing the correlation between the unshod and shod horse in overall GRF patterns showed that there was a high positive correlation between the craniocaudal GRF patterns (with a maximum correlation coefficient of 0.994 with a 2% lag of the shod pattern). These results also showed a high positive correlation between the vertical GRF patterns (with a maximum correlation coefficient of 0.996 with a 0% lag of the shod pattern). While there also seemed to be a large similarity in mediolateral GRF patterns, the strength of the positive correlation was lower than in the other directions (with a maximum correlation coefficient of 0.747 with an 11% lag of the shod pattern).

The craniocaudal GRF at the beginning of the stance phase moved caudally and shifted cranially from mid-stance until the end of the stance phase of locomotion (Figure 3). The maximum cranial GRF for the shod horse was shown at approximately 75% of stance (497N) and for the unshod horse at 78% of stance (396N). Between 75-78% of stance, the shod horse showed on average a 21% higher craniocaudal GRF than the unshod horse.

The mediolateral GRF for the shod condition moved medially throughout the whole stance phase and reached a maximum of approximately 80N after mid-stance. Contrastingly, the mediolateral GRF for the unshod horse moved medially only at the beginning of the stance phase and shifted laterally from around 10% of stance until late mid-stance and then moved medially until the end of the stance phase. The highest mediolateral GRF for the unshod horse was before mid-stance (~40-45%), reaching approximately 100N.

There was a strong similarity in the vertical GRF pattern between the shod and unshod conditions at the beginning and towards the end of the stance phase. At mid-stance, the vertical GRF of the shod condition was approximately 3195N, 10% higher than the unshod horse (2888N).

Kinematic Data

The kinematic data for the shod (n=4) and unshod (n=4) conditions during the stance phase of locomotion are shown in Figure 4 and Supplementary Data 3. The results from the cross-correlation analysis between the unshod and shod conditions showed a high positive correlation for the PIP mean joint angle (with a maximum correlation coefficient of 0.989 with a 0% lag of the shod pattern). A strong positive correlation was also found for the DIP mean joint angle (with a maximum correlation coefficient of 0.975 with a 0% lag of the shod pattern).

We describe some differences in kinematic patterns here for the shod vs. unshod conditions but it is very important to note that none of these have true statistical significance, because of the small sample sizes. Overall, in both the shod and unshod conditions, the PIP joint extended between 10 - 40% of the stance phase and flexed before mid-stance (45% of stance) until the end of the stance phase (90%). In particular, the PIP joint for the shod conditions had 45% higher total range of motion than the unshod horse.

The DIP mean joint angle at 10% of the stance phase was extended more in the unshod (6.4°) than the shod (3.5°) condition. A similar pattern of greater extension of the DIP joint for the unshod condition was observed until the 25% of the stance phase, after which the shod DIP joint extended more; however, the differences in extension between the shod and unshod conditions were minimal and not truly significant. The maximum difference between the DIP joint angle in the shod and unshod conditions was at 40% of stance, when the DIP joint of the shod condition was extended, whilst the DIP of the unshod horse was flexed. At mid-stance and until the end of the stance phase, the DIP was flexed in both the shod and unshod conditions (Table 2). Overall the DIP joint of the shod condition had higher range of motion than the unshod condition by 23%.

Finite Element Analysis (FEA)

The intersegmental forces assigned to the shod and unshod conditions for the FEA are in Table 3. Our FEA results showed that the shoe increased the concentration of von Mises stresses on the dorsal (Figure 5) and ventral (Figure 6) aspects of the distal (P1, P2, P3) bones of the horse's forefoot (Supplementary Data 4). Specifically, the shod horse had respectively 20%, 27% and 20% higher von Mises stresses for the P1, P2 and P3 vs. the unshod horse (Figure 7 and Table 4). In both the shod and unshod conditions, the highest concentration of stresses was on the dorsal aspect of the distal epiphysis for the P1, at the midshaft both cranially and dorsally for the P2 and on the cranial aspect of the P3.

Discussion

Our study utilized a new combination of XROMM, inverse dynamics modelling and FEA to quantify the effect of wearing a stainless steel shoe on the biomechanics of the right forefoot of a Thoroughbred horse during slow walking, although admittedly our small sample sizes preclude conclusive detection of any statistically significant differences. Our kinetic analysis showed an increase in the craniocaudal, mediolateral and vertical GRFs in particular at the mid-stance phase of stance and this finding is in accord with previous studies in Thoroughbred (Roepstorff, Johnston & Drevemo 1999) and Warmblood horses (Willeman, Savelberg & Barneveld 1998). The reported differences in GRFs between the shod and unshod horse may be due to the grip or impact attenuation properties of the shoe material. Previous studies have reported that horseshoe materials have variable frictional and damping properties and can affect the dynamics of the foot in horses (Heidt et al., 1996; Wilson et al., 1992; Pardoe et al., 2001). It is thus possible that an increase in the craniocaudal GRF may be due to the gripping properties of the steel shoe when in contact with the experimental platform, which could shorten the slip time and increase musculoskeletal forces after impact (Willemen 1997; Johnston et al., 1995).

Joint kinematics data was consistent with our expectations for a cursorial animal such as our horse subject. During the stance phase in both shod and unshod conditions, the horse's forefoot joints flexed and extended by large amounts but minimal motion occurred in adduction-abduction and longitudinal rotation. This finding corresponds to those from previous kinematic studies on unshod horses during walking that also reported flexion-extension as the dominant rotation and only minimal adduction-abduction and longitudinal rotations (Clayton et al., 2007a; Clayton et al., 2007b). The negligible rotational differences between the shod and the unshod conditions during longitudinal rotation and adduction-abduction found in our study likely are confounded not only by our small sample sizes but also by noise due to the very small rotations and human error in rotoscoping such fine details of motion. Menegaz et al.'s (2015) kinematic study on pig feeding also attributed minimal rotations that failed to pass their precision threshold to noise introduced by the XROMM analysis procedure.

Our kinematic data for both the shod and unshod conditions showed extension at both the PIP and DIP joints at approximately 10% of stance until mid-stance and flexion during late stance, just before the foot leaves the ground. This finding is consistent with previous studies of horse foot kinematics in both walking and trotting, which have shown that the PIP and DIP joints maintain a similar motion pattern in those gaits, with changes evident only in the amounts of rotation (Chateau, Degueurce & Denoix 2004; Clayton et al., 2007b). Whilst the greater flexion of the DIP joint relative to the PIP joint after mid-stance and at late stance is in accord with previous research on walking and trotting horses in shod and unshod conditions (Clayton et al., 2007b; Roach et al., 2015; Roepstorff, Johnston & Drevemo 1999), our study did not record extension of either the PIP or the DIP joints after the mid-stance phase of stance. This may be due to individual behaviour of the horse we used in our analysis and/or the limited space the animal walked on, and is complicated by our small sample size. Although the horse received training prior to data collection, walking on a platform surrounded by equipment could have intimidated the animal and thereby influenced its natural locomotor behaviour and speed. Future research should measure more individuals to account for intraspecific variations in locomotor behaviours. A constraint on this sort of multi-individual study, however, is that each individual must have its distal limb CT or MRI scanned to obtain subject-specific morphological data for XROMM analysis, which requires mild sedation, anaesthesia or euthanasia, with accompanying ethical dilemmas and risks, in addition to the very time-intensive nature of not only collecting synchronised kinematic and kinetic data but also processing the XROMM data and subject-specific musculoskeletal (e.g. Opensim) and FEA modelling analyses. Hence, despite our study's restriction to measurement of one individual and a few steps, it is an important example of the integration of 3D biomechanical methods and their application to fundamental problems in equine locomotion, care and welfare.

Our results do not show distinct differences in the PIP and DIP ranges of motion during the step (although our small sample prevented detection of any differences that might have been present), which concurs with the notion that it seems unlikely that different shoe materials induce horses to modify their gait (Pardoe et al., 2001). On the contrary, our FEA results revealed an increase in the von Mises bone stress magnitudes in the shod (vs. unshod) horse's forefoot phalanges at mid-stance. Both conditions showed increased stresses on the distal epiphysis of the proximal phalanx in the dorsal and ventral view. The unshod horse showed slightly higher stresses than the shod horse around the sagittal groove of the P1, yet stresses around this area were low compared to the midshaft and the proximal epiphysis. This finding is partly similar to those presented by O'Hare et al., (2013) during walking, yet their study found higher stresses around the sagittal groove of the proximal phalanx. This is potentially due the fact that the proximal distal force that was assigned to the O'Hare et al., (2013) model to simulate walk was 3600N, whilst our inverse dynamics analysis resulted in 2503N and 2354N for the shod and unshod conditions respectively. In addition our model is solid, stiffer and thus will have smaller responses to stress.

Our FEA results also showed an increase in von Mises stresses around the midshaft of the intermediate phalanx and around the proximal borders of the navicular bone, yet in both the shod and unshod conditions stresses around the navicular bone were minimal. It is possible that the navicular bone acts more of a lever for the deep digital flexor tendon (DDFT) (Eliashar, McGuigan and Wilson 2004), rather than in load-bearing yet a more advanced model that includes the deep and superficial digital flexor tendons is required to precisely assess whether increases of tendon stresses is a compensatory mechanism to keep navicular bone stresses low.

Our preliminary finding that the shod horse has higher stress concentrations on the distal fore foot than the unshod horse, coupled with the increased GRFs in the shod condition, indicates that the steel shoe likely increased mechanical loading and potentially reduced the ability of the hoof to expand and dissipate stresses. The mechanism by which the loaded hoof expands has been contrastingly explained by the "pressure theory" and "depression theory". Whilst the pressure theory contends that the pressure in the frog of the hoof accounts for heel expansion (Colles, 1989; Roepstorff, Johnston & Drevemo 2001), the depression theory proposes that heel expansion is due to the depression of the hoof caused by the backward rotation of the intermediate phalanx (Dyhre-Poulsen et al., 1994; Roepstorff, Johnston & Drevemo 2001).

According to the depression theory, one would expect that the typical DIP joint angle would decrease (i.e. involving a more plantarflexed coffin [DIP] joint) from the unshod to shod condition, limiting the expansion of the heel in the shod condition and consequently increasing bone stresses. Our results support this hypothesis up until mid-stance, showing that the mean DIP joint angle decreased from the unshod to shod conditions, yet after mid-stance the mean DIP rotation increased from unshod to shod, so our overall findings on this issue are inconclusive. It remains possible that the shoe constrains the backward tilting (plantarflexion) of the intermediate phalanx, constrains the depression and thus expansion of the hoof and thus increases bone stresses at mid-stance, but more data are needed to test this hypothesis. To test the pressure theory, we would need to include the soft tissues of the hoof, especially the frog, in our FEA and test if the stress in the frog is appreciably higher in the shod condition.

There is also the valid concern that, whilst our experimental data (kinematics and kinetics) are *in vivo* measurements of real motions and have a high degree of precision, our OpenSim and FEA modelling analyses did not account for the tissues of the hooves themselves, the shoes, ligaments, tendons, frog or other soft tissues that would certainly alter the mechanics of the foot. Thus our analysis shows what the influence of shod vs. unshod conditions of our horse subject were solely upon the *in vivo* dynamics (including the altered GRFs and motions) and upon the stresses within the bones in the theoretical case of those bones bearing all loads themselves. Certainly the absolute values of the stresses would change with the addition of soft tissue data and neuromuscular control, but it is less certain how much the relative stresses would change between the shod vs. unshod conditions. Regardless, this will remain unknown until more sophisticated models are created and additional studies are conducted. Even so, we have presented the first analysis that integrates state-of-the-art methods for kinematic and kinetic analysis with musculoskeletal modelling and finite element analysis methods for the distal foot of horses, which itself is a considerable methodological advance that future studies can build upon.

Our preliminary study illustrates that the stainless steel shoe may influence the dynamics and mechanics of a Thoroughbred horse’s forefoot during slow walking, although our results are inconclusive in some important aspects. Certainly, more research is needed to quantify the effect of the shoe on the equine forefoot during the whole stance phase, under different trimming protocols, at faster speeds/gaits and with more individuals and strides as well as a similar focus on the hindfeet. Expansion of this research question, especially via the application of this novel combination of in vivo experiments and computer models should not only create a foundation of stronger data and inferences on which future studies can continue to build, but can also bolster confidence in equine biomechanics to better understand the form, function and pathological relationships of the anatomical tissues of the equine foot.

Acknowledgements

We thank Sharon Warner, Renate Weller, Luis Lamas, Emily Sparkes, Heather Paxton and Julia Molnar for their assistance and technical support during data collection. We also thank Phil

Pickering for his assistance with the setup of the custom-made platform and the fluoroscopy system and Justin Perkins for allowing us access to the Thoroughbred horse. We are grateful to Sandra Shefelbine and Andrea Pereira for useful discussions on FEA and our colleagues at the University of Brown (Sabine Moritz, David Baier and Beth Brainerd) for their endless support during the processing of the XROMM data. Particular thanks are also due to Todd Pataky and Vivian Allen for valuable discussions.

References

Alexander RMcN, Jayes AS. 1983. A dynamic similarity hypothesis for the gaits of quadrupedal mammals. *Journal of Zoology* 201:135-152.

Ault B, Starling G, Parkes R, Pfau T, Pardoe C, Day P, Bettison C, Weller R. 2015. The effect of three different shoeing conditions on tendon strain in the thoroughbred forelimb. *Equine Veterinary Journal* 47: 17. DOI: 10.1111/evj.12486_39.

Baier DB, Gatesy SM. 2013. Three-dimensional skeletal kinematics of the shoulder girdle and forelimb in walking Alligator. *Journal of Anatomy* 223: 462-73.

Baier DB, Gatesy SM, Dial KP. 2013. Three-Dimensional, High-Resolution Skeletal Kinematics of the Avian Wing and Shoulder during Ascending Flapping Flight and Uphill Flap-Running. *PLoS ONE* , 8(5): e63982. Doi:10.1371/journal.pone.0063982.

Bailey CJ, Reid SW, Hodgson DR, Rose RJ. 1999. Impact of injuries and disease on a cohort of two- and threeyear-old Thoroughbreds in training. *Veterinary Record* 145: 487-93.

Bowker RM, Atkinson PJ, Atkinson TS, Haut RC. 2001. Effect of contact stress in bones of the distal interphalangeal joint on microscopic changes in articular cartilage and ligaments. *American Journal of Veterinary Research* 62:414–424.

Brainerd EL, Baier DB, Gatesy SM, Hedrick TL, Metzger KA, Gilbert SL, Crisco JJ. 2010. X-ray reconstruction of moving morphology (XROMM): precision, accuracy and applications in comparative biomechanics research. *Journal of Experimental Zoology. Part A, Ecological Genetics and Physiology* 313A: 262–279.

Chateau H, Degueurce C, Denoix J-M. 2004. Evaluation of three-dimensional kinematics of the distal portion of the forelimb in horses walking in a straight line. *American Journal of Veterinary Research* 65: 447–455.

Clayton HM, Sha DH, Stick JA, Elvin N. 2007a. 3D kinematics of the equine metacarpophalangeal joint at walk and trot. *Veterinary and Comparative Orthopaedics and Traumatology* 20: 86–91.

Clayton HM, Sha DH, Stick JA, Robinson P. 2007b. 3D kinematics of the interphalangeal joints in the forelimb of walking and trotting horses. *Veterinary and Comparative Orthopaedics and Traumatology* 20: 1–7.

Clayton HM, Sha DH, Stick JA, Mullineaux DR. 2004. Three dimensional kinematics of the equine carpus at trot. *Equine Veterinary Journal* 36: 671–676.

Clegg PD. 2011. Musculoskeletal disease and injury, now and in the future. Part 1. Fractures and fatalities. *Equine Veterinary Journal* 43 (6): 643-649.

Cogger N, Evans D, Perkins N, Hodgson D, Reid S. 2006. Risk Factors for injuries in Thoroughbred Horses. A report for the Rural Industries Research and Development Corporation. Australia Government, Rural Industries Research and Development Corporation *RIRDC Publication No 06/050.*

Colles C. 1989. The relationship *of* frog pressure to heel expansion. *Equine Veterinary Journal* 21: 13-16.

Collins SN, Murray RC, Kneissl S, Stanek C, Hinterhofer C. 2009. Thirty-two component finite element models of a horse and donkey digit. Equine Veterinary Journal 41(3): 219-224.

Dawson MM, Metzger KA, Baier DB, Brainerd EL. 2011. Kinematics of the quadrate bone during feeding in Mallard ducks. *Journal of Experimental Biology* 214: 2036-2046.

Delp SL., Anderson FC, Arnold AS, Loan P, Habib A, John C T, Guendelman E, Thelen DG. 2007. OpenSim: Open-Source Software to Create and Analyze Dynamic Simulations of Movement. *IEEE Transactions on Biomedical Engineering* 54: 11.

Dobbert T. 2005. *Matchmoving: the invisible art of camera tracking*. Alameda, CA: Sybex

Douglas JE, Biddick TL, Thomason JJ, Jofriet JC. 1998. Stress/strain behaviour in the laminar junction. *Journal of Experimental Biology* 201:2287–2297.

Dyce KM, Sack WO, Wensing CJG. 2010. Textbook of Veterinary Anatomy (fourth edition). Saunders Elsevier

Dyhre-Poulsen P, Smedegaard HH, Roed J, Korsgaard E.1994. Equine hoof function investigated by pressure transducers inside the hoof and accelerometers mounted on the first phalanx. *Equine Veterinary Journal* 26:362-366.

Eliashar E, McGuigan MP, Wilson AM. Relationship of foot conformation and force applied to the navicular bone of sound horses at the trot 2004. *Equine Veterinary Journal* 36:431-435.

Foote C, McIntosh A, V'Landys P, Bulloch K. 2011. *Health and Safety in Australian Horse Racing. Canberra, Australia: ACT*

Gatesy SM, Baier DB, Jenkins FA, Dial KP. 2010. Scientific rotoscoping: a morphology-based method of 3-D motion analysis and visualization. *Journal of Experimental Zoology Part A: Ecology Genetics and Physiology* 313A: 244–261.

Gidmark NJ, Konow N, LoPresti E, Brainerd EL 2013. Bite force is limited by the force-length relationship of skeletal muscle in black carp, *Mylopharyngodon piceus*. *Biology Letters* 9:20121181.

Gidmark NJ, Staab KL, Hernandez LP, Brainerd EL 2012. Flexibility in starting posture drives flexibility in kinematic behavior of the kinethmoid-mediated premaxillary protrusion mechanism in a cyprinid fish, *Cyprinus carpio*. *Journal of Experimental Biology* 215: 2262-2272.

Heidt RSJr, Dormer SG, Cawley PW, Scranton PE Jr, Losse G, Howard M. 1996. Differences in frictional and torsional resistance in athletic shoe-turf interfaces. *American Journal of Sports Medicine 24:*834-842.

Hinterhofer C, Stanek C, Haider H. 2001. Finite element analysis (FEA) as a model to predict effects of farriery on the equine hoof. *Equine Veterinary Journal* 33:58–62.

Hinterhofer C, Stanek C, Binder K. 1998. Elastic modulus of equine hoof horn, tested in wall samples, sole samples and frog samples at varying levels of moisture. Berl Munchener Tierarzt Wochenschrift 111:217–221.

Hutton DV. 2003. *Fundamentals of finite element analysis*. McGraw-Hill Inc. New York.

Jansová M, Ondoková L, Vychytil J, Kochová P, Witter K, Tonar Z. 2015. A finite element model of an equine hoof. *Journal of Equine Veterinary Science* 35: 60-69.

Jeffcott LB, Rossdale PD, Freestone J, Frank CJ, Towers-Clark PF. 1982. An assessment of wastage in thoroughbred racing from conception to 4 years of age. *Equine Veterinary Journal* 14: 185-198.

Johnston C, Roepstorff L, Drevemo S, Kallings P. 1995. Kinematics of the distal forelimb during the stance phase in the fast trotting Standardbred. *Equine Veterinary Journal*., *Suppl.* 18: 170-174.

Jordan P, Willneff J, D'Apuzzo N, Weishaupt M, Wistner T, Auer J. 2001. Photogrammetric measurement of deformations of horse hoof horn capsules. In *Videometrics and optical methods for 3D* shape measurements, Proc SPIE, 4309: 204–11.

Lundberg A, Goldie I, Kalin B, Selvik G. 1989. Kinematics of the ankle/foot complex: plantarflexion and dorsiflexion. *Foot & Ankle International* 9: 194–200.

McClinchey HL, Thomason JJ, Jofriet JC. 2003. Isolating the effects of equine hoof shape measurements on capsule strain with finiteelement analysis. *Veterinary and Comparative Orthopaedics and Traumatology* 16:67–75.

McKee SL. 1995. An update on racing fatalities in the UK. Equine Veterinary Education 7(4): 202-204.

Menegaz RA, Baier DB, Metzer KA, Herring SW, Brainerd EL. (2015). XROMM analysis of tooth occlusion and temporomandibular joint kinematics during feeding in juvenile miniature pigs. *Journal of Experimental Biology* 218:2573-2584. Doi: 10.1242/jeb.119438

Metzger KA, Baier DB, Lin A, Harper CJ, Herring SW. 2009. XROMM analysis of mastication in miniature pigs. *Integrative and Comparative Biology*. 49(Suppl 1): e115

Miranda DL, Rainbow MJ, Crisco JJ, Fleming BC. 2013. Kinematic differences between optical motion capture and biplanar videoradiography during a jump-cut maneuver. *Journal of Biomechanics* 46(3):567-573.

Moyer W, Anderson JP. 1975. Lameness caused by improper shoeing. *Journal of American Veterinary Medical Association* 166:47-52.

Nyakature JA, Fischer MS. 2010. Three-dimensional kinematic analysis of the pectoral girdle during upside-down locomotion of two-toed sloths (Choloepus didactylus, Linné 1758). *Frontiers in Zoology* 7:21.

O'Hare LMS, Cox PG, Jeffery N, Singer ER. 2013. Finite element analysis of stress in the equine proximal phalanx. Equine Veterinary Journal DOI: 10.1111/j.2042-306.2012.00635.x.

Pardoe CH, McGuigan MP, Rogers KM, Rowe LL, Wilson AM. 2001. The effect of shoe material on the kinetics and kinematics of foot slip at impact on concrete. *Equine Veterinary Journal* 33: 70-73.

Parkin TD, Clegg PD, French NP, Proudman CJ, Riggs CM, Singer ER, Webbon PM, Morgan KL. 2004. Risk of fatal distal limb fractures among Thoroughbreds involved in the five types of racing in the United Kingdom. *Veterinary Record* 154: 493-497.

Reinschmidt C, van den Bogert AJ, Murphy N, Lundberg A, Nigg BM. 1997. Tibiocalcaneal motion during running, measured with external and bone markers. Clinical Biomechanics 12: 8–16.

Rho JY, Currey JD, Zioupos P, Pharr GM. 2001. The anisotropic Young's modulus of equine secondary osteons and interstitial bone determined by nanoindentation. *The Journal of Experimental Biology* 204:1774-1781.

Roach JM, Pfau T, Bryars J, Unt V, Channon SB, Weller R. 2015. Sagittal distal limb kinematics inside the hoof capsule captured using high-speed fluoroscopy in walking and trotting horses. *The Veterinary Journal.* DOI: 10.1016/j.tvjl.2014.06.014.

Roepstorff L, Johnston C, Drevemo S. 1999. The effect of shoeing on kinetics and kinematics during the stance phase. *Equine Veterinary Journal* 31 (Suppl. 30): 279–285.

Roepstorff L, Johnston C, Drevemo S. 2001. In vivo and in vitro heel expansion in relation to shoeing and frog pressure. *Equine Veterinary Journal* 33: 54-57.

Salo Z, Runciman RJ, Thomason JJ. 2009. A dynamic model of a horse hoof at first contact. *Biosystems Engineering* 103: 364-373.

Thomason JJ, Douglas JE, Sears W. 2001. Morphology of the laminar junction in relation to the shape of the hoof capsule and third phalanx in adult horses (Equus caballus). *Cells Tissues Organs* 166:304–318.

Thomason JJ, McClinchey HL, Jofriet JC. 2002. The analysis of strain and stress in the equine hoof capsule using finite-element methods: comparison with principal strains recorded in vivo. *Equine Veterinary Journal* 34:719–725.

Thomason JJ, McClinchey HL, Faramarzi B, Jofriet JC. 2005. Mechanical behavior and quantitative morphology of the equine laminar junction. *The anatomical record. Part A, Discoveries in molecular, cellular, and evolutionary biology* 283(2): 366–79.

van Heel MC, Moleman M, Barneveld A, van Weeren, Back W.2005. Changes in location of centre of pressure and hoof-unrollment pattern in relation to an 8-week shoeing interval in the horse. *Equine Veterinary Journal* 37: 536-40.

van Heel MC, van Weeren PR, Back W. 2006. Compensation for changes in hoof conformation between shoeing sessions through the adaptation of angular kinematics of the distal segments of the limbs of horses. *American Journal of Veterinary Research* 67:1199-1203.

van Weeren PR, van den Bogert AJ, Barneveld A. 1990. A quantitative analysis of skin displacement in the trotting horse. *Equine Veterinary Journal* S9: 101–109.

Wang J, Blackburn TJ. 2000. The AARM/RSNA physics tutorial for residents: x-ray image intensifiers for fluoroscopy. *Radiographics* 20:1471–1477.

Willemen MA. 1997. *Horseshoeing, a Biomechanical Analysis*. PhD Thesis, University of Utrecht.

Willemen MA, Savelberg HHCM, Barneveld A. 1998. The improvement of the gait quality of sound trotting warmblood horses by normal shoeing and its effect on the load on the lower forelimb. *Livestock Production Science* 52: 145–153.

Wilson PD, Ratzlaff MH, Grant BD, Hyde ML, Balch OK. 1992. The effects of a compressible plastic shoe-the seattle shoe-on the kinematics of the strides of galloping thoroughbred horses. *Journal of Equine Veterinary Science* 12 (6): 374-381.

Witte TH, Knill K, Wilson AM. 2004. Determination of peak vertical ground reaction force from duty factor in the horse (Equus caballus). *Journal of Experimental Biology* 207: 3639-3648.

Figure Captions

Figure 1. A. Experimental set-up of the horse walking on a custom-made platform retrofitted with a force plate and surrounded by the bi-planar fluoroscopy system. B. Virtual setup of the horse right forefoot based on the experimental alignment of the x-ray sources and the intensifiers. Images in black frames (right and left) illustrate the reflections of the distal foot from the two x-ray cameras.

Figure 2. XROMM model with bone segments and coordinate systems for the metacarpophalangeal (MCP), proximal interphalangeal (PIP) and distal interphalangeal (DIP) joints. Red, green and blue arrows represent the x, y and z segment axes respectively.

Figure 3. Ground reaction forces normalised to 100% stance phase for the shod (black lines) and unshod horse (red lines). For the craniocaudal GRF, cranial and caudal are positive and negative respectively. For the mediolateral GRF, medial is positive and lateral is negative. Solid lines represent the trials used in the subsequent finite element analysis.

Figure 4. Degrees of rotation for the proximal interphalangeal (PIP) and distal interphalangeal (DIP) joints, around the flexion (negative) - extension (positive) axes during the stance phase for the shod (black line) and the unshod (red line) conditions. Dotted lines show the individual trials and the bold lines show the mean degrees of rotation for each condition.

Figure 5. Von Mises stress distribution results for the shod and the unshod horse foot, in dorsal view. Bones shown from left to right are the P1, P2 and P3. Warm (red) and cold (blue) colours show higher and lower von Mises stresses respectively.

Figure 6. Von Mises stress distribution results for the shod and the unshod horse foot, in ventral view. Bones shown from left to right are the P1, P2 and P3. Warm (red) and cold (blue) colours show higher and lower von Mises stresses respectively.

Figure 7. Von Mises stresses presented as numerical results for the P1, P2 and P3. Note that no differences can be considered to be statistically significant.

Supplementary Figures

Figure S1. The position of the custom-designed calibration cube used during the fluoroscopy experiments to calibrate the 3D space in the XROMM analysis.

Figure S2. Loading and boundary locations for the P1, P2 and P3 bones (see Methods: Loads and constraints).

Figure S3. Regional definitions (in red) for the P1 (A), P2 (B) and P3 (C) bones. All external and internal nodes of the midshaft were selected and nodal von Mises stresses were exported for the comparisons within homologous bones and both the shod and unshod conditions.

Supplementary Movies

Movie S1. Animation of the shod horse during walking (Trial 9).

Movie S2. Animation of the unshod horse during walking (Trial 54).

Supplementary Data Captions

Supplementary Data 1. Raw speed data for the unshod (n=4) and shod (n=4) conditions. Column A shows the conditions. Column B lists the name and date of the steps. Column C lists the horse's hip height in meters. Column D lists the frame rate of the Sony camera used for the speed calculations. Columns E and F list the start and end frame of each trial and each condition. Column G shows the difference between the start and end frame (i.e. number of frames elapsed). Column H shows the time in seconds and was calculated by dividing 1 over the camera frame rate (column D), multiplied by the frame difference (column G). Column I shows the distance that a marker placed on the middle of the body of the horse travelled between the start and end frames of the steps (columns E and F). Column J lists the velocity calculations per trial and condition. Velocity was measured by dividing the distance (column I) over the time (column H). Column K lists gravity at $9.81 ms^{-2}$ and column L lists the Froude number per trial and condition. Rows J6 and J 12 show the average velocity for the unshod and shod condition respectively. Rows L6 and L12 show the average Froude number for the unshod and shod conditions respectively.

Supplementary Data 2. Ground reaction force (GRF) data in Newtons for the unshod (n=4) and shod (n=4) conditions.

Supplementary Data 3. Degrees of motion for proximal interphalangeal (PIP) and distal interphalangeal (DIP) joints for the shod (n=4) and unshod (n=4) conditions about the flexion-extension axis.

Supplementary Data 4. Raw von Mises stress data (MPa) for each condition and each bone segment. Bone segments are defined as the proximal phalanx (P1), intermediate phalanx (P2) and distal phalanx (P3). All stress data were exported from the external and internal nodes of the midshaft from homologous locations between bones and conditions as per Figure S3.

Table 1(on next page)

Tables 1-3

Table 1. Minimum (Min), maximum (Max) and mean Froude number and velocity data, with standard deviation (SD), for the shod (n=4) and unshod (n=4) horse trials.

Condition	*n*	**Froude number**			
		Min	**Max**	**Mean**	**SD**
SHOD	4	0.045	0.076	0.058	0.013
UNSHOD	4	0.060	0.069	0.064	0.0045
Condition	*n*	**Velocity (ms^{-1})**			
		Min	**Max**	**Mean**	**SD**
SHOD	4	0.64	0.83	0.72	0.079
UNSHOD	4	0.74	0.79	0.76	0.024

Table 2. Mean degrees of rotation for the proximal interphalangeal (PIP) and distal interphalangeal (DIP) joints of the shod and unshod conditions during the stance phase. Note that none of these differences can be considered statistically significant.

	PIP		**DIP**	
% Stance	**UNSHOD**	**SHOD**	**UNSHOD**	**SHOD**
10	5.1	6.3	6.4	3.5
15	5.2	5.8	6.7	4.1
20	4.6	4.7	6.3	4.4
25	3.5	3.3	5.1	4.4
30	2.4	1.8	3.5	3.8
35	1.3	0.7	1.6	3.1
40	0.3	-0.5	-0.3	1.9
45	-0.6	-1.8	-2	0.1
50	-1.5	-2.9	-3.6	-2.8
55	-2.4	-3.9	-5.2	-6
60	-3.3	-5.1	-6.6	-9.1
65	-4.2	-6.1	-8.4	-12.5
70	-5.4	-7	-10.6	-15.9
75	-6.4	-7.5	-13.7	-19.3
80	-7.1	-7.5	-18.8	-22.4
85	-7.2	-7.3	-23.7	-24.4
90	-5.8	-6.8	-25.7	-25

Table 3. Intersegmental forces in Newtons (N) assigned to the shod and unshod horse finite element models.

	Proximal-Distal		Medial-lateral		Cranial-caudal	
Force	**Shod**	**Unshod**	**Shod**	**Unshod**	**Shod**	**Unshod**
PIP	2503	2354	-2024	-1492	48	199
DIP	2580	2293	-1924	-1583	47	200

Table 4. Regional von Mises stress data for the shod and unshod conditions, with mean % difference from shod to unshod conditions shown. Note that none of these differences can be considered statistically significant.

Bone	**Model**	**von Mises stress (MPa)**				**% Difference**
		Mean	Min	Max	SD	
SHOD	P1	10.5	1.5	48.0	7.4	-20.3
UNSHOD	P1	8.7	1.2	40.7	6.1	
SHOD	P2	5.7	1.1	16.5	2.2	-27.4
UNSHOD	P2	4.4	0.9	12.8	1.7	
SHOD	P3	7.7	0.0	22.5	4.5	-20.0
UNSHOD	P3	6.4	0.0	19.8	3.7	

Figure 1(on next page)

A. Experimental set-up of the horse walking on a custom-made platform retrofitted with a force plate and surrounded by the bi-planar fluoroscopy system.

B. Virtual setup of the horse right forefoot based on the experimental alignment of the x-ray sources and the intensifiers. Images in black frames (right and left) illustrate the reflections of the distal foot from the two x-ray cameras.

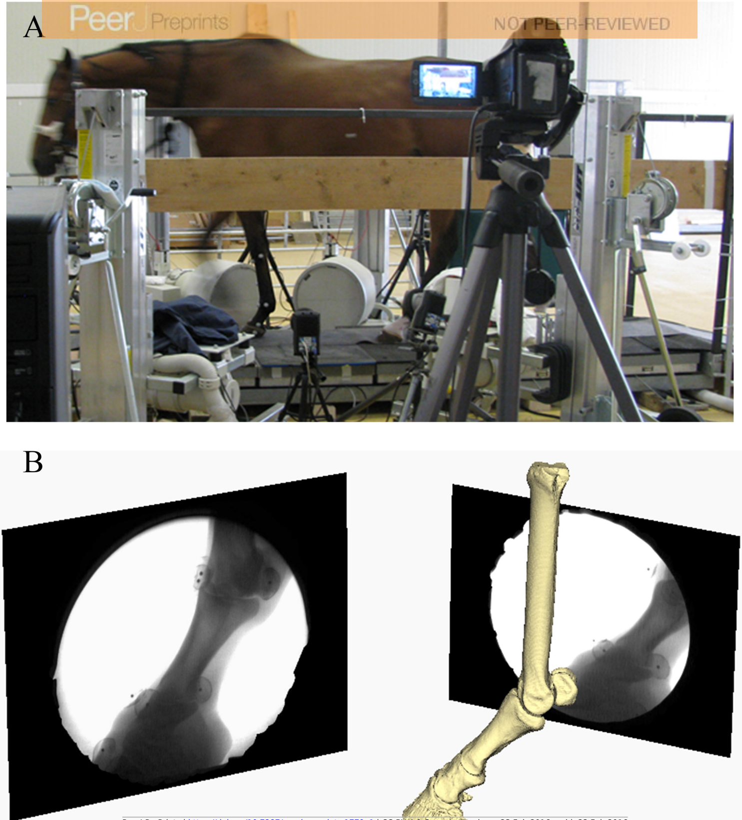
A
B

2

XROMM model with bone segments and coordinate systems for the metacarpophalangeal (MCP), proximal interphalangeal (PIP) and distal interphalangeal (DIP) joints.

Red, green and blue arrows represent the x, y and z segment axes respectively.

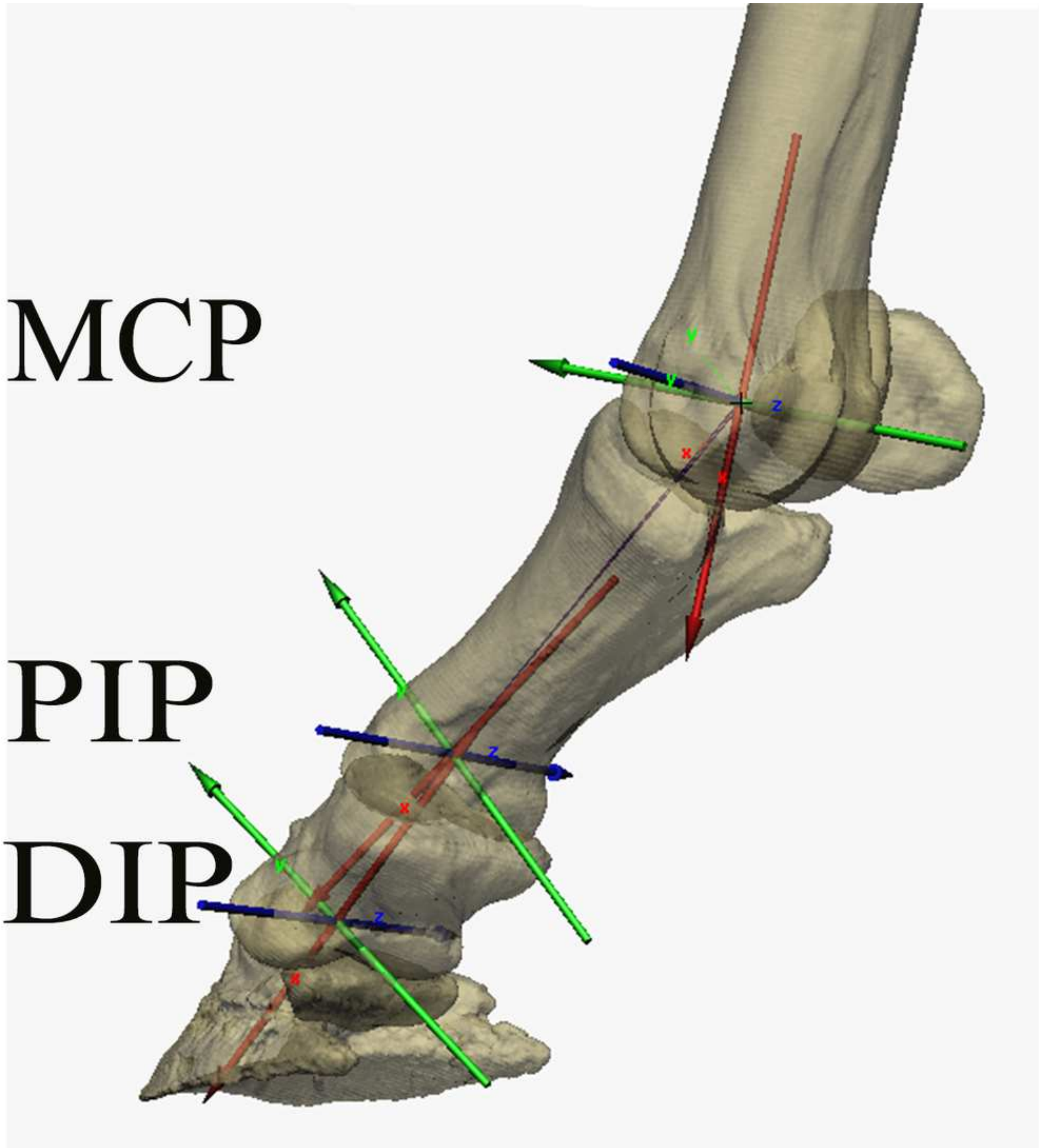

3

Ground reaction forces normalised to 100% stance phase for the shod (black lines) and unshod horse (red lines).

For the craniocaudal GRF, cranial and caudal are positive and negative respectively. For the mediolateral GRF, medial is positive and lateral is negative. Solid lines represent the trials used in the subsequent finite element analysis.

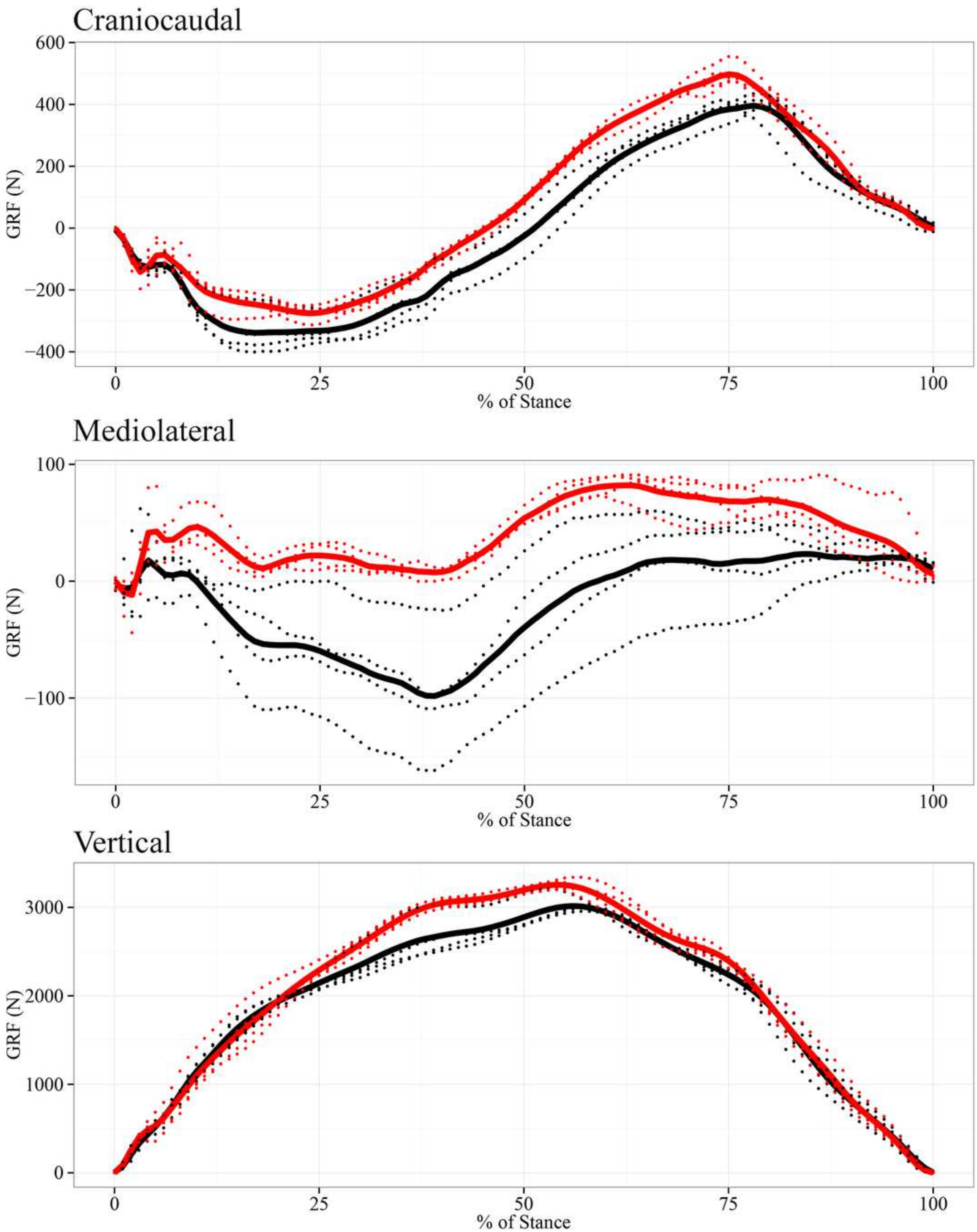

PeerJ PrePrints | https://doi.org/10.7287/peerj.preprints.1779v1 | CC-BY 4.0 Open Access | rec: 23 Feb 2016, publ: 23 Feb 2016

4

Joint Kinematics.

Degrees of rotation for the proximal interphalangeal (PIP) and distal interphalangeal (DIP) joints, around the flexion (negative) - extension (positive) axes during the stance phase for the shod (black line) and the unshod (red line) conditions. Dotted lines show the individual trials and the bold lines show the mean degrees of rotation for each condition.

PeerJ PrePrints | https://doi.org/10.7287/peerj.preprints.1779v1 | CC-BY 4.0 Open Access | rec: 23 Feb 2016, publ: 23 Feb 2016

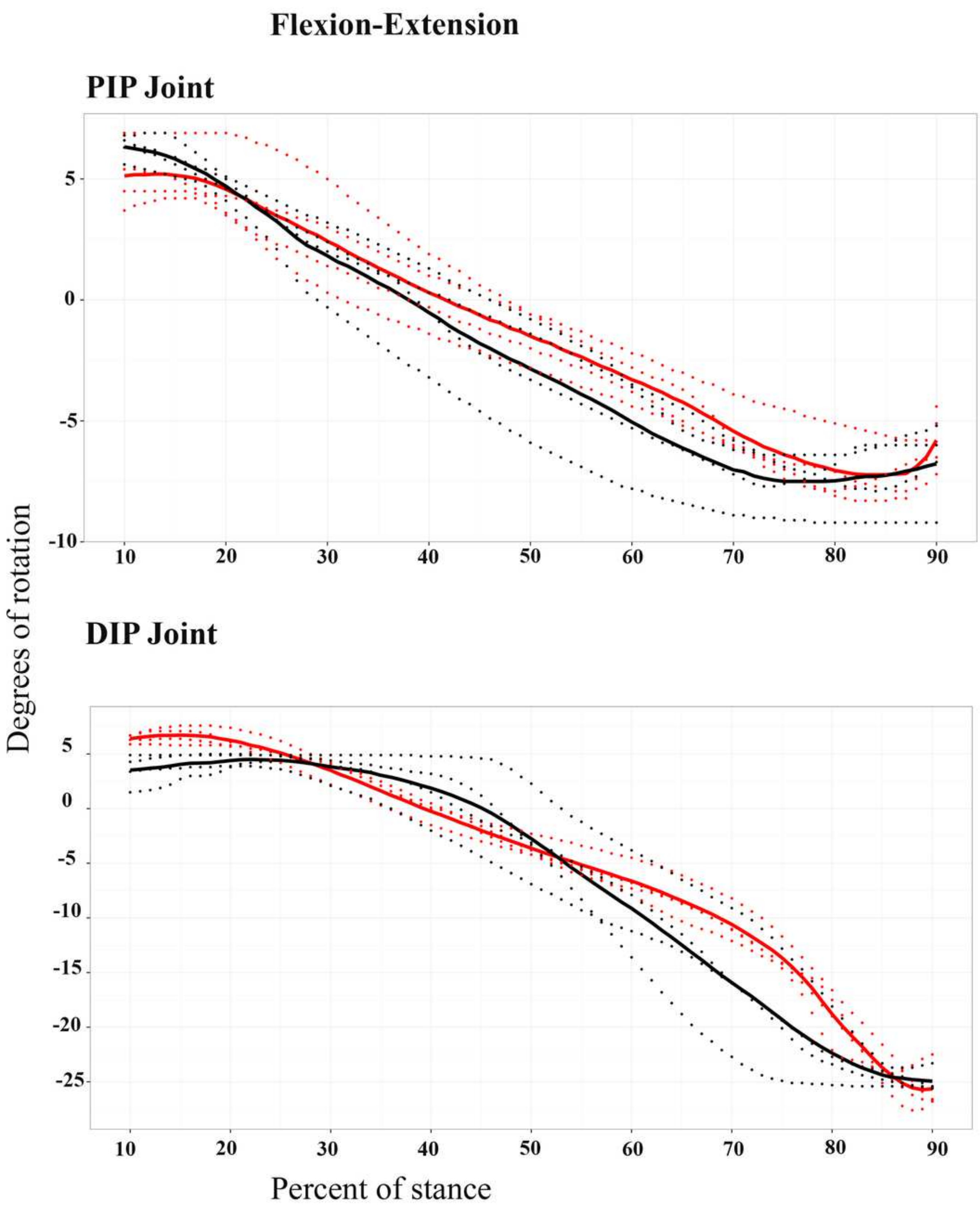
Flexion-Extension
PIP Joint
5
0
-5
-10
10
20
30
40
50
60
70
80
90
DIP Joint
5
0
-5
-10
-15
-20
-25
10
20
30
40
50
60
70
80
90
Degrees of rotation
Percent of stance

5

Von Mises stress distribution results for the shod and the unshod horse foot, in dorsal view.

Bones shown from left to right are the P1, P2 and P3. Warm (red) and cold (blue) colours show higher and lower von Mises stresses respectively.

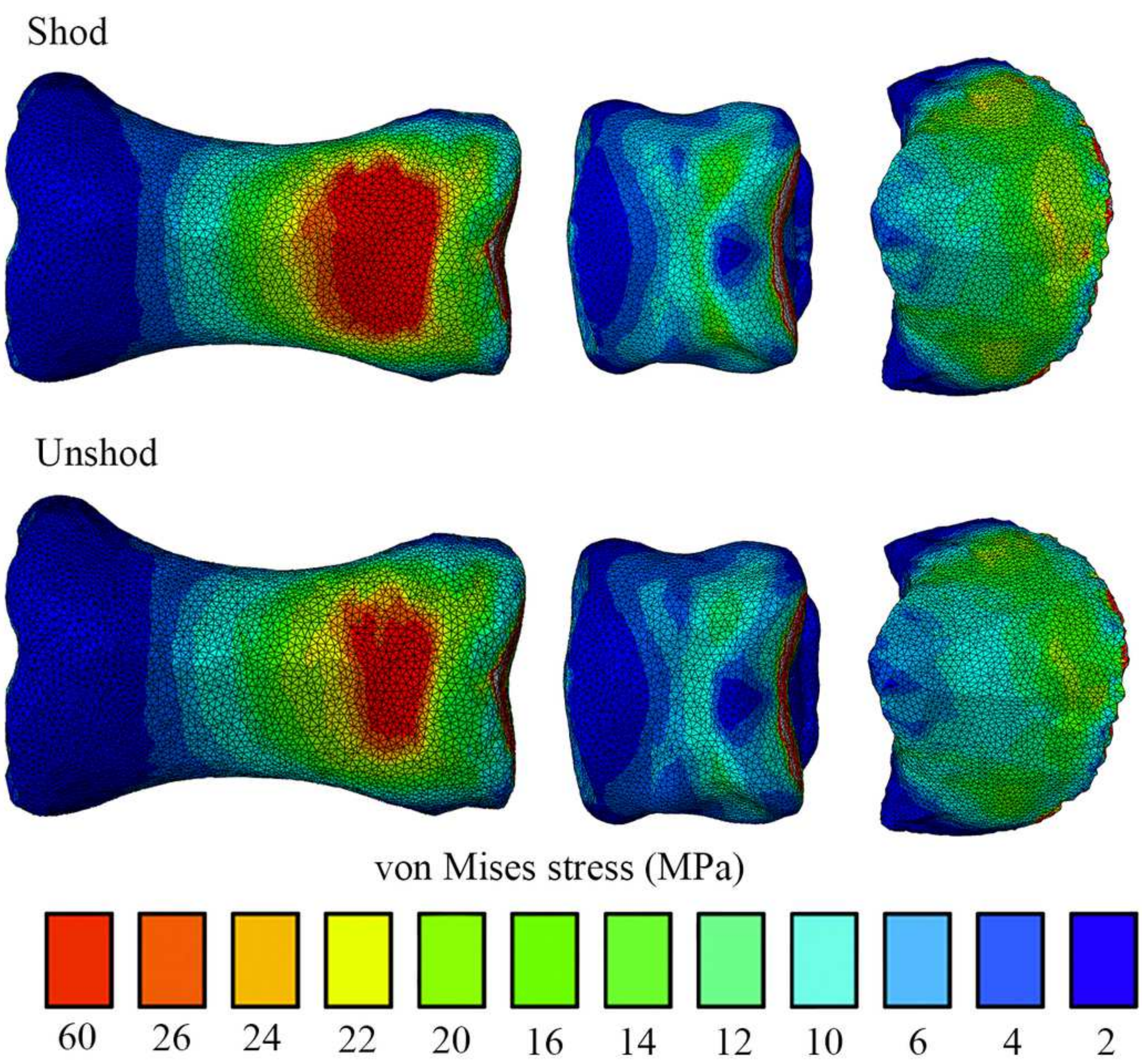

6

Von Mises stress distribution results for the shod and the unshod horse foot, in ventral view.

Bones shown from left to right are the P1, P2 and P3. Warm (red) and cold (blue) colours show higher and lower von Mises stresses respectively.

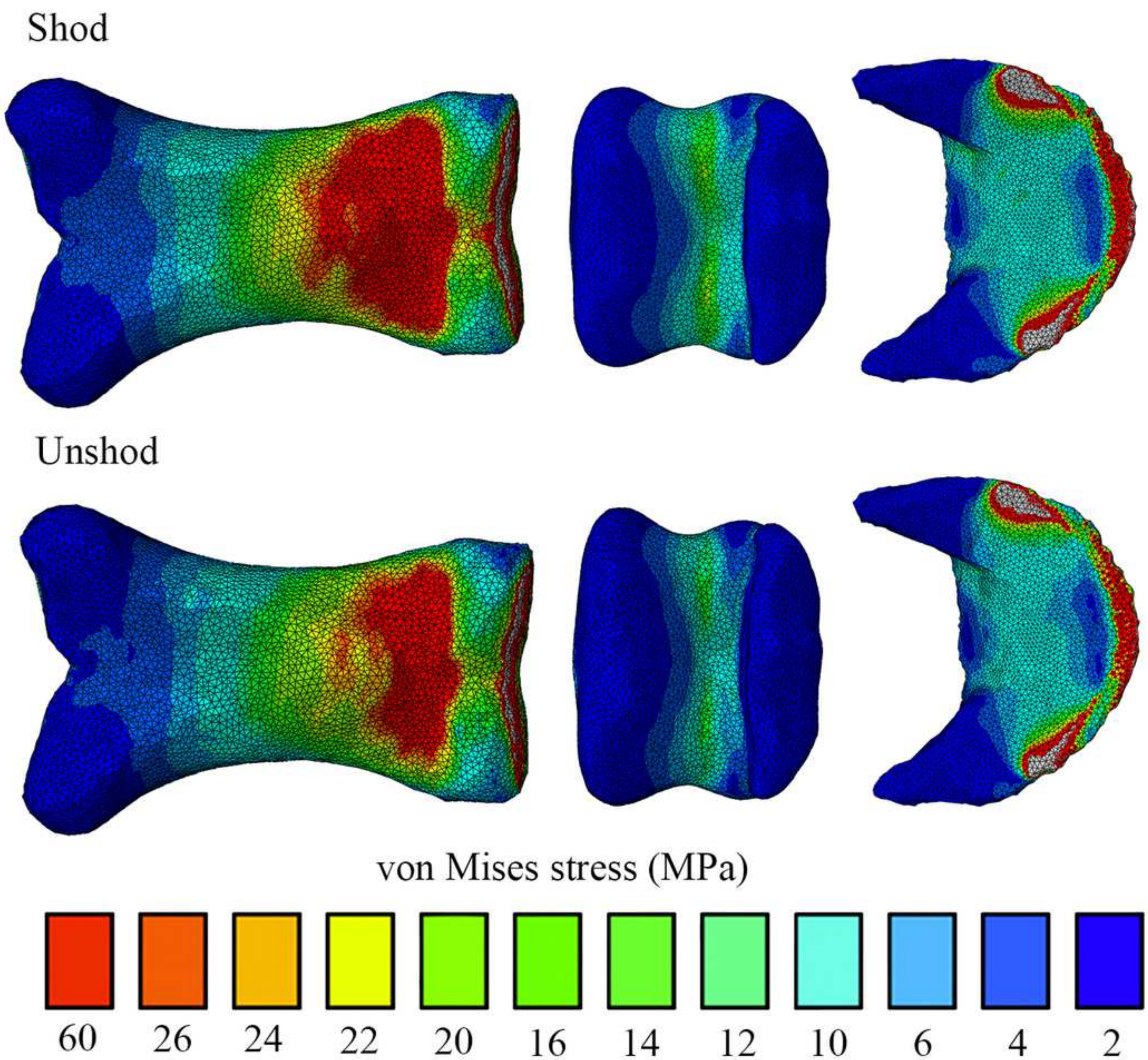

7

Von Mises stresses presented as numerical results for the P1, P2 and P3. Note that no differences can be considered to be statistically significant.